Evidence for superconductivity in Li-decorated monolayer graphene

B. M. Ludbrook[a,b], G. Levy[a,b], P. Nigge[a,b], M. Zonno[a,b], M. Schneider[a,b], D. J. Dvorak[a,b], C. N. Veenstra[a,b], S. Zhdanovich[b,c], D. Wong[a,b], P. Dosanjh[a,b], C. Straßer[d], A. Stöhr[d], S. Forti[d], C. R. Ast[d], U. Starke[d], and A. Damascelli[a,b,1]

[a]Department of Physics and Astronomy, University of British Columbia, Vancouver, BC V6T 1Z1, Canada; [b]Quantum Matter Institute, University of British Columbia, Vancouver, BC V6T 1Z4, Canada; [c]Department of Chemistry, University of British Columbia, Vancouver, BC V6T 1Z1, Canada; and [d]Max Planck Institute for Solid State Research, 70569 Stuttgart, Germany

Monolayer graphene exhibits many spectacular electronic properties, with superconductivity being arguably the most notable exception. It was theoretically proposed that superconductivity might be induced by enhancing the electron–phonon coupling through the decoration of graphene with an alkali adatom superlattice [Profeta G, Calandra M, Mauri F (2012) Nat Phys 8(2):131–134]. Although experiments have shown an adatom-induced enhancement of the electron–phonon coupling, superconductivity has never been observed. Using angle-resolved photoemission spectroscopy (ARPES), we show that lithium deposited on graphene at low temperature strongly modifies the phonon density of states, leading to an enhancement of the electron–phonon coupling of up to $\lambda \simeq 0.58$. On part of the graphene-derived π^*-band Fermi surface, we then observe the opening of a $\Delta \simeq 0.9$-meV temperature-dependent pairing gap. This result suggests for the first time, to our knowledge, that Li-decorated monolayer graphene is indeed superconducting, with $T_c \simeq 5.9$ K.

graphene | superconductivity | ARPES

Although not observed in pure bulk graphite, superconductivity occurs in certain graphite intercalated compounds (GICs), with T_c values of up to 11.5 K in the case of CaC_6 (1, 2). The origin of superconductivity in these materials has been identified in the enhancement of electron–phonon coupling induced by the intercalant layers (3, 4). The observation of a superconducting gap on the graphitic π^*-bands in bulk CaC_6 (5) suggests that realizing superconductivity in monolayer graphene might be a real possibility. This prospect has, indeed, attracted intense theoretical and experimental efforts (6–12). In particular, recent density functional theory calculations have suggested that, analogous to the case of intercalated bulk graphite, superconductivity can be induced in monolayer graphene through the adsorption of certain alkali metals (8).

Although the Li-based GIC—bulk LiC_6—is not known to be superconducting, Li-decorated graphene emerges as a particularly interesting case with a predicted superconducting T_c of up to 8.1 K (8). The proposed mechanism for this enhancement of T_c is the removal of the confining potential of the graphite C_6 layers, which changes both the occupancy of the Li 2s band (or the ionization of the Li) and its position with respect to the graphene layer. These modifications lead to an increase of the electron–phonon coupling constant from $\lambda = 0.33$ to $\lambda = 0.61$, in going from bulk to monolayer LiC_6. It has been argued that the LiC_6 monolayer should exhibit the largest values of both λ and T_c among all alkali–metal–C_6 superlattices (8). Nevertheless, although there is thorough experimental evidence for adatom-enhanced electron–phonon coupling in graphene (7, 11, 13), superconductivity has not yet been observed in decorated monolayer graphene.

Angle-resolved photoemission spectroscopy (ARPES) measurements of the electronic dispersion of pristine and Li-decorated graphene at 8 K, characterized by the distinctive Dirac cones at the corners of the hexagonal Brillouin zone (Fig. 1E), are shown in Fig. 1 A and B. Li adatoms electron-dope the graphene sheet by charge transfer doping, leading to a shift of the Dirac point to higher

binding energies. As evidenced by the evolution of the graphene sheet carrier density in Fig. 1F, this trend begins to saturate after several minutes of Li deposition. Concomitantly, we observe the emergence of a new spectral weight (Fig. 1E) at the Brillouin zone center (the comparison of the Γ-point ARPES dispersion for pristine and 10-min Li-decorated graphene is shown in Fig. 1 C and D). The origin of this spectral weight is probably the Li-2s band expected for this system (8) superimposed with the folded graphene bands caused by a Li superstructure, which were observed in Li and Ca bulk GIC systems (5, 14). This spectral weight, which disappears above ∼ 50 K and is not recovered on subsequent cooling, is associated with the strong enhancement of electron–phonon coupling (discussed later, see Fig. 3 and *SI Appendix*).

Next, we use high-resolution, low-temperature ARPES to search for the opening of a temperature-dependent pairing gap along the π^*-band Fermi surface as a direct spectroscopic signature of the realization of a superconducting state in monolayer LiC_6. To increase our experimental sensitivity, as illustrated in Fig. 2A, using the approach introduced for FeAs (17) and cuprate (18) superconductors, we perform an analysis of ARPES energy distribution curves (EDCs) integrated in dk along a 1D momentum–space cut perpendicular to the Fermi surface. This method also provides the added benefit that the integrated EDCs can be modeled in terms of a simple Dynes gap function (19) multiplied by a linear background and the Fermi–Dirac distribution, all convolved with a Gaussian resolution function (*Methods* and Eq. 4). As shown in Fig. 2A and especially, Fig. 2B, for data from the k-space location indicated by

Significance

Although superconductivity is well-known in intercalated bulk graphite, the ultimate goal of inducing superconductivity in single-layer graphene has not yet been achieved. We have here developed an experiment that combines ultralow-temperature (5 K) and ultrahigh-vacuum (10^{-11} torr) sample preparation with high-resolution angle-resolved photoemission spectroscopy (ARPES). We show that decorating monolayer graphene with a layer of lithium atoms enhances the electron–phonon coupling to the point where a superconducting state can be stabilized at low temperature. Measurements of the size of the superconducting gap by ARPES suggest a T_c of about 5.9 K. This result constitutes the first observation, to our knowledge, of superconductivity in monolayer graphene. Given the massive scientific and technological interest in graphene, our findings will have significant cross-disciplinary impact.
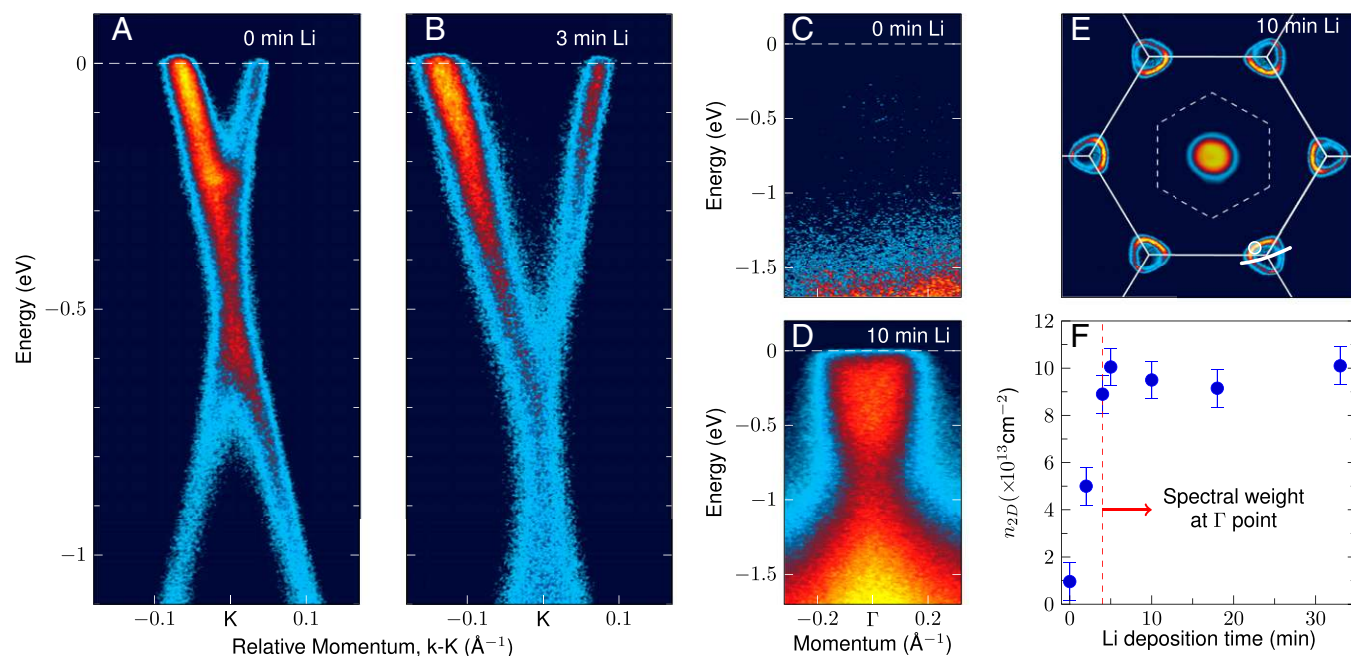
PHYSICS

Fig. 1. Charge transfer doping of graphene by lithium adatoms. Dirac-cone dispersion measured by ARPES at 8 K (*A*) on pristine graphene and (*B*) after 3 min of Li evaporation along the *K*-point momentum cut indicated by the white line in the Fermi surface plot in *E*. The Dirac cone–Fermi surface was measured at this specific *K* point and then replicated at the other *K* points by symmetry (note that high-symmetry points are here defined for the Brillouin zone of pristine graphene and not of $\sqrt{3} \times \sqrt{3}R30°$ reconstructed Li-graphene, which is, instead, the notation in ref. 8). The point at which the spectroscopic gap is studied is indicated by the shaded white circle. The Dirac point, (*A*) already located below E_F on pristine graphene because of the charge transfer from the SiC substrate, further shifts to higher energies with (*B*) Li evaporation. The presence of a single well-defined Dirac cone indicates a macroscopically uniform Li-induced doping. (*C*) Although no bands are present at the Γ-point on pristine graphene, spectral weight is detected on 10-min Li-decorated graphene in *D* and *E*. As illustrated in the 8 *K* sheet carrier density plot vs. Li deposition time in *F*, which accounts for the filling of the π^* Fermi surface, the spectral weight at Γ is observed for charge densities $n_{2D} \gtrsim 9 \times 10^{13}$ cm^{-2} (but completely disappears if the sample temperature is raised above ~ 50 K and is not recovered on subsequent cooling) (*SI Appendix*).
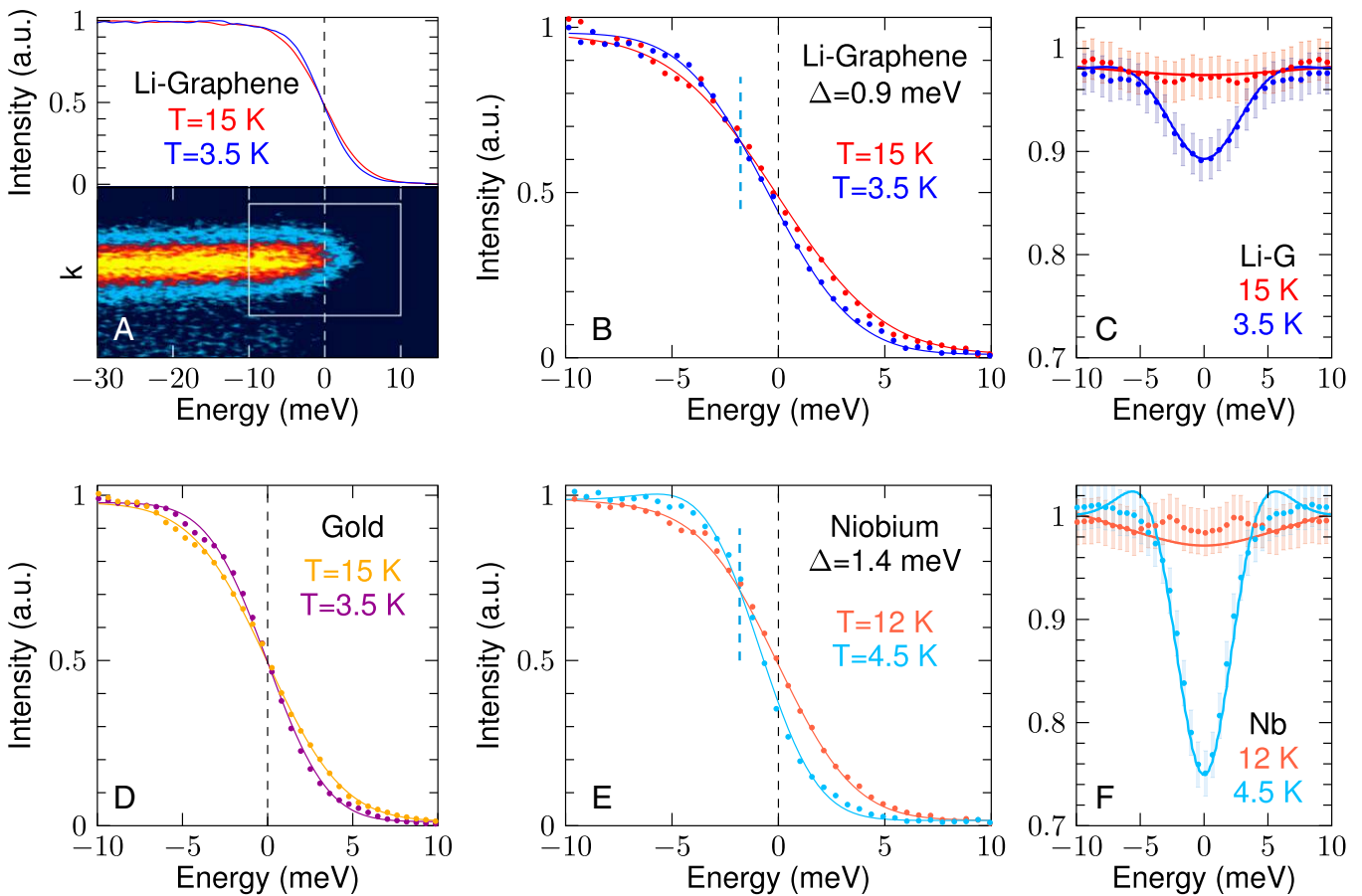
the white circles in Figs. 1*E* and 3*E*, a temperature dependence characteristic of the opening of a pairing gap can be observed near E_F. The leading-edge midpoints of the Li-graphene spectra move away from E_F (Fig. 2*B*) in cooling from 15 to 3.5 K, which is at variance with the case of Au spectra crossing precisely at E_F according to the Fermi–Dirac distribution (Fig. 2*D*). Fitting these data with Eq. **4** returns a gap value of $\Delta = 0.9 \pm 0.2$ meV at 3.5 K (with $\Gamma \simeq 0.09$ meV). [Note that the parameter Γ in the Dynes fitting function is not treated as a free-fitting parameter, because the broadening of the coherence peaks and filling in of the gap are dominated by the experimental energy resolution. However, setting this parameter to small realistic values ($\Gamma \sim 0.1\Delta$) improves the fit at the center of the gap (i.e., at $E = 0$ in the symmetrized data) without affecting the value of the gap itself.] Given its small value compared with the experimental resolution, the gap opening is best visualized in the symmetrized data in Fig. 2*C*, which minimize the effects of the Fermi function. Finally, we note that the gap appears to be anisotropic and is either absent or below our detection limit along the $K - M$ direction (*SI Appendix*, Fig. S4).

The detection of a temperature-dependent anisotropic gap at the Fermi level with a leading-edge profile described by the Dynes function—with its asymmetry about E_F and associated transfer of spectral weight to just below the gap edge—is suggestive of a superconducting pairing gap. The phenomenology would, in fact, be very different in the case of a Coulomb gap, which is typically observed in disordered semiconductors (23–25) because of the combination of disorder with long-range Coulomb interactions. A Coulomb gap would lead to a rigid shift of the spectra leading edge (isotropic in momentum) and result in a vanishing of the momentum-integrated density of states at E_F. Similarly, the observed gap is unlikely to have a charge density wave origin, because the observed gap is tied to the Fermi energy

as opposed to a particular high-symmetry wavevector (the latter might occur at the *M* points, when graphene is doped all of the way to the Van Hove singularity, resulting in a highly nested hexagonal Fermi surface; or the *K* points, in the case of a $\sqrt{3} \times \sqrt{3} R$ 30° reconstruction, leading to a Dirac point gap). Finally, we note that these measurements do not allow us to speculate on the precise symmetry of the gap along a single Dirac cone–Fermi surface or the relative phases of the gap on the six disconnected Fermi pockets. As such, our results do not rule out any of the recent proposals for a possible unconventional super-conducting order parameter in graphene (9, 26, 27).

To further explore the nature of the gap observed on Li-decorated graphene (and also show our ability to resolve a gap of the order of 1 meV), in Fig. 2 *E* and *F*, we show as a benchmark comparison the analogous results from a bulk polycrystalline niobium sample—a known conventional superconductor with $T_c \simeq 9.2$ K. The Dynes fit of the integrated EDCs Fermi edge in Fig. 2*E* determines the gap to be $\Delta = 1.4 \pm 0.2$ meV (with $\Gamma \simeq 0.14$ meV), in excellent agreement with reported values (28). Although the leading-edge shift (Fig. 2*E*) and the dip in the symmetrized spectra (Fig. 2*F*) are more pronounced than for Li-graphene owing to the larger gap, the behavior is qualitatively very similar. This similarity provides additional support to the superconducting origin of the temperature-dependent gap observed in Li-decorated graphene.

If the spectroscopic gap observed in Li-graphene is, indeed, a superconducting gap, the responsible mechanism may likely be electron–phonon coupling, which was predicted by the theory for monolayer Li-graphene (8) and also, seen experimentally for the bulk GIC CaC$_6$ (5). In direct support of this scenario, we present a detailed analysis of the graphene π^*-bands in Fig. 3, showing that the Li-induced enhancement of the electron–phonon coupling

Ludbrook et al.

Fig. 2. Spectroscopic observation of a pairing gap in Li-decorated graphene. (*A*) Dirac dispersion from 10-min Li-decorated graphene measured at 15 and 3.5 K at the *k*-space location indicated by the white circles in Figs. 1*E* and 3*E*; the temperature dependence is here evaluated for EDCs integrated in the 0.1-Å⁻¹ momentum region about k_F shown by the white box in *Lower*, with (*Upper*) the only changes occurring near E_F. (*D*) Although Au spectra cross at E_f as described by the Fermi–Dirac distribution, (*B*) the crossing points of the Li-graphene spectra are shifted away from E_F (cyan dashed line) because of the pull back of the leading edge at 3.5 K. A fit to the Dynes gap equation (*Methods*) yields a gap of $\Delta \simeq 0.9$ meV at 3.5 K (and 0 meV at 15 K). The superconducting gap opening is best visualized in the symmetrized data in *C* [i.e., by taking $I(\omega) + I(-\omega)$, which minimizes the effects of the Fermi function, even in the case of finite energy and momentum resolutions (15, 16); blue and red symbols in *C* represent the smoothed data, whereas the light shading gives the rmsds of the raw data]. The qualitatively similar behavior observed on polycrystalline niobium—and returning a superconducting gap $\Delta \simeq 1.4$ meV—is shown in *E* and *F*.

is, indeed, sufficient to stabilize a low-temperature superconducting state. Graphene doped with alkali adatoms always shows a strong kink in the π^*-band dispersion at a binding energy of about 160 meV (11). For the Li-graphene studied here, the same effect is seen in the momentum distribution curve (MDC) dispersions and the corresponding real part of the self-energy Σ' in Fig. 3 *B–D*. This structure stems from the coupling to carbon in-plane (C_{xy}) phonons (4, 8). Despite the apparent strength of this kink, the interaction with these phonon modes contributes little to the overall coupling parameter because of their high energy (note that ω is a weighting factor in the integral calculation of λ) (*Methods*). As illustrated by the white circles in Fig. 3*I*, the contribution to λ from these high-energy (100–200 meV) modes is determined to be 0.14 ± 0.05, and it remains approximately constant for all Li coverages studied here. This value is, however, too small to stabilize a superconducting state in this system (8, 11).

With increasing Li coverage and the appearance of the spectral weight at Γ, significant modifications to the low-energy part of the dispersion ($\lesssim 100$ meV) become apparent (Fig. 3 *B–D*). With 10 min of Li deposition (Fig. 3*D*), an additional kink is visible at a binding energy of ~30 meV along with the associated peak in the real part of the self-energy Σ'. The extracted (*Methods*) Eliashberg functions and energy-resolved $\lambda(\omega)$ in Fig.

3 *F–H* show that, at high Li coverage, phonon modes at energies below 60 meV are coupling strongly to the graphene electronic excitations. The phonon modes in this energy range are of Li in-plane (Li_{xy}) and C out-of-plane (C_z) character (4, 8). This assignment is in agreement with predictions (8) as shown by the direct comparison between theory and experiment in Fig. 3*H*. [As for the theoretical and experimental Eliashberg functions $\alpha^2 F(k, \omega)$ in Fig. 3*H*, the agreement may, at first glance, appear not as good as the one for $\lambda(\omega)$. We note, however, that, in this regard, the relevant information is in the macroscopic energy distribution of the $\alpha^2 F(k, \omega)$ weight rather than in its detailed structure.] As for the total electron–phonon coupling λ for each coverage (black circles in Fig. 3*I*), our values measured on the π^*-band Fermi surface at an intermediate location between $\Gamma - K$ and $K - M$ directions (Fig. 3*E*) provide an effective estimate for the momentum-averaged coupling strength. [The electron–phonon coupling parameter increases monotonically along the π^*-band Fermi surface in going from the $\Gamma - K$ to the $K - M$ direction as observed in both decorated graphene (11) and intercalated graphite (29). Empirically, the value measured at the intermediate Fermi crossing corresponds to the momentum-averaged coupling strength along the π^*-band Fermi surface.] Remarkably, the value $\lambda = 0.58 \pm 0.05$ observed at the highest Li coverage
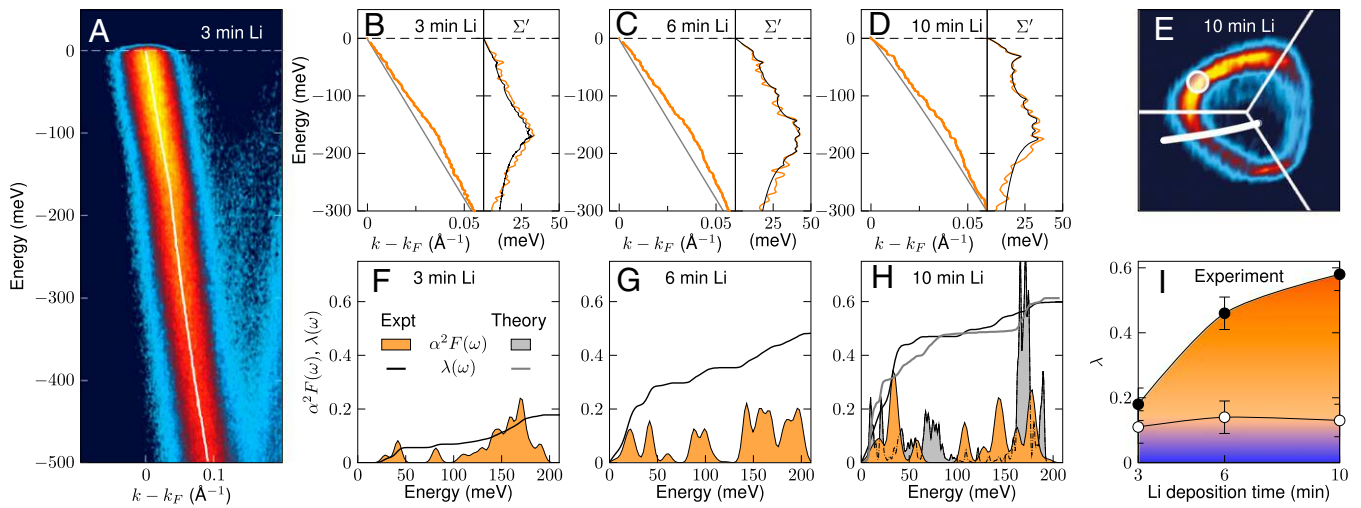
Fig. 3. Analysis of electron–phonon coupling in Li-decorated graphene. (A) Dirac dispersion from 3-min Li-decorated graphene along the k-space cut indicated in the Fermi surface plot in E that exhibits kink anomalies caused by electron–phonon coupling (white line indicates MDC dispersion). (B–D) MDC dispersion and bare bands obtained from the self-consistent Kramers–Kronig bare-band fitting (KKBF) routine (20, 21) for several Li coverages (*Methods* and *SI Appendix*); the real part of the self-energy Σ' is shown in *Right* (orange indicates Σ' from the KKBF routine analysis, and black indicates Σ' corresponding to the Eliashberg function presented below). (F–H) Eliashberg function $\alpha^2 F(\omega)$ from the integral inversion of $\Sigma'(\omega)$ (22) and electron–phonon coupling constant $\lambda = 2 \int d\omega \, \alpha^2 F(\omega)/\omega$ (*Methods* and *SI Appendix*); in H, the theoretical results from ref. 8 for a LiC$_6$ monolayer are also shown (gray shading). (I) Experimentally determined contribution to the total electron–phonon coupling (black circles) from phonon modes in the energy ranges 100–250 meV (blue shading and white circles) and 0–100 meV (orange shading); the coupling of low-energy modes strongly increases with Li coverage.

(Fig. 3I) is comparable with $\lambda = 0.61$ predicted for monolayer LiC$_6$ (8) as well as $\lambda \simeq 0.58$ observed for bulk CaC$_6$ (29)—it is, thus, large enough for inducing superconductivity in Li-decorated graphene. It is also significantly larger than the momentum-averaged results previously reported for both Li and Ca depositions on monolayer graphene [$\lambda \simeq 0.22$ and $\lambda \simeq 0.28$, respectively (11)]. We note that achieving such a large λ-value is critically dependent on the presence of the spectral weight observed at Γ when Li is deposited on graphene at low temperatures, presumably forming an ordered structure on the surface and not intercalating. As shown in *SI Appendix*, we find $\lambda = 0.13 \pm 0.05$ after the same sample is annealed at 60 K for several minutes, destroying the Li order and associated Γ-spectral weight.

Taken together, our ARPES study of Li-decorated monolayer graphene provides evidence for the presence of a temperature-dependent pairing gap on part of the graphene-derived π^* Fermi surface. The detailed evolution of the density of states at the gap edge as well as the phenomenology analogous to the one of known superconductors, such as Nb—as well as CaC$_6$ and NbSe$_2$, which also show a similarly anisotropic gap around the K point (30–34)—indicate that the pairing gap observed at 3.5 K in graphene is most likely associated with superconductivity. Based on the Bardeen–Cooper–Schrieffer gap equation, $\Delta = 3.5 \, k_b \, T_c$, we estimate a superconducting transition temperature $T_c \simeq 5.9$ K, remarkably close to the value of 8.1 K found in density functional theory calculations (8). This work constitutes the first, to our knowledge, experimental realization of superconductivity in graphene—the most prominent electronic phenomenon still missing among the remarkable properties of this single layer of carbon atoms.

Methods

Sample Preparation. Epitaxial graphene monolayers with a carbon buffer layer were grown under argon atmosphere on hydrogen-etched 6H-SiC(0001) substrates as described in ref. 35. The samples were annealed at 500 °C and 8×10^{-10} torr for 1 h immediately before the ARPES measurements. Lithium adatoms were deposited from a commercial SAES alkali metal source, with the graphene samples held at a temperature of 8 K. Bulk Nb polycrystalline samples, with $T_c = 9.2$ K, were cleaved in the ARPES chamber before the experiments.

ARPES Experiments. The measurements were performed at the University of British Columbia with s-polarized 21.2-eV photons on an ARPES spectrometer equipped with a SPECS Phoibos 150 Hemispherical Analyzer, a SPECS UVS300 Monochromatized Gas Discharge Lamp, and a six-axes cryogenic manipulator that allows for controlling the sample temperature between 300 and 3.5 K, with accuracy ±0.1 K. Band and Fermi surface mapping as well as the study of electron–phonon coupling were performed at 8 K, with energy and angular resolution set to 15 meV and 0.01 Å^{-1}, respectively. For the measurements of the superconducting gaps, energy and angular resolution were set to 6 meV and 0.01 Å^{-1}, and the sample temperature was varied between 3.5 and 15 K. During the ARPES measurement, the chamber pressure was better than 4×10^{-11} torr.

Electron–Phonon Coupling Analysis. The spectral function $A(\mathbf{k}, \omega)$ measured by ARPES (36) provides information on both the single-particle electronic dispersion $\varepsilon_{\mathbf{k}}^b$ (the so-called "bare band") and the quasiparticle self-energy $\Sigma(\mathbf{k}, \omega) = \Sigma'(\mathbf{k}, \omega) + i\Sigma''(\mathbf{k}, \omega)$, which have real and imaginary parts that account for the renormalization of electron energy and lifetime caused by many-body interactions, including electron–phonon coupling. By fitting with a Lorentzian and a constant background, the ARPES intensity profiles at constant energy $\omega = \bar{\omega}$ known as MDCs, one obtains the MDC dispersion defined by the peak maximum k_m (plotted in Fig. 3 A–D) as well as the corresponding half-width half-maximum Δk_m. The real and imaginary parts of the self-energy can then be defined as

$$\Sigma'_{\bar{\omega}} = \bar{\omega} - \varepsilon_{k_m}^b$$
$$\Sigma''_{\bar{\omega}} = -\Delta k_m v_{k_m}^b,$$

$$[1]$$

where $v_{k_m}^b$ is the bare-band velocity. To extract the self-energy and dispersion without any a priori knowledge of the bare band, we use the self-consistent Kramers–Kronig bare-band fitting routine from refs. 20 and 21 (*SI Appendix*). As for the dimensionless k-resolved electron–phonon coupling constant discussed in the paper and particularly, Fig. 3 F–I, this quantity is formally defined as (37)

$$\lambda_{\mathbf{k}}(\omega) = 2 \int_0^\omega d\omega' \, \frac{\alpha^2 F(\mathbf{k}, \omega')}{\omega'},$$

$$[2]$$

where $\alpha^2 F(\mathbf{k}, \omega)$ is the Eliashberg function [i.e., the phonon density of states weighted by the electron–phonon coupling strength (37)]. The latter is related to the real part of the self-energy $\Sigma'(\mathbf{k}, \omega)$ through the integral relation

$$\Sigma'(\mathbf{k}, \omega) = \int_0^\infty d\omega' \alpha^2 F(\mathbf{k}, \omega') \; K\left(\frac{\omega}{kT}, \frac{\omega'}{kT}\right), \qquad \textbf{[3]}$$

where $K(y, y') = \int_{-\infty}^{+\infty} dx \; f(x-y) \; 2y'/(x^2 - y'^2)$ and $f(x-y)$ is the Fermi–Dirac distribution. The momentum resolved $\alpha^2 F(\mathbf{k}, \omega)$ function plotted in Fig. 3 *F–H* can then be extracted from the real part of the self-energy $\Sigma'(\mathbf{k}, \omega)$ probed by ARPES by the integral inversion procedure described in ref. 22. Ultimately, by means of Eq. **2**, this approach also allows the calculation of the electron–phonon coupling constant shown in Fig. 3 (*SI Appendix*).

Superconducting Gap Fitting. As discussed in detail for the cases of FeAs and cuprate superconductors in refs. 17 and 18, respectively, when evaluating the opening of a superconducting gap based on the EDCs integrated in *dk* along a 1D momentum–space cut perpendicular to the Fermi surface (such as those presented in Fig. 2), one can make use of the following formula:

$$I_{\int dk}(\omega) = \left[f(\omega, T) \; (a + b \; \omega) \left| \mathrm{Re} \frac{\omega - i\Gamma}{\sqrt{(\omega - i\Gamma)^2 - \Delta^2}} \right| \right] \otimes R_\omega . \qquad \textbf{[4]}$$

This equation corresponds to the Dynes gap function [i.e., the Bardeen–Cooper–Schrieffer density of states with a superconducting gap Δ broadened by the pair-breaking scattering rate Γ (19)] multiplied by a linear background (with parameters *a* and *b*) and the Fermi–Dirac distribution

$f(\omega, T)$ all convolved with a Gaussian function R_ω accounting for the experimental energy resolution [owing to the integration of the ARPES intensity in *dk*, this analysis is unaffected by momentum resolution (17)]. The high- and low-temperature ARPES data in Fig. 2 are fitted simultaneously using the above equation according to the following additional considerations. Because the integrated EDCs were observed not to change outside of the gap region, the linear background is constrained to be the same for the above and below T_c measurements. The temperatures are fixed to the known measured values (with accuracy ±0.1 K). The Fermi energy E_F and energy resolution are determined from fitting the high-temperature data from either Nb or Li-graphene during each measurement and independently verified from measurements on polycrystalline gold.

1. Emery N, et al. (2005) Superconductivity of bulk CaC6. *Phys Rev Lett* 95(8):087003.
2. Weller TE, Ellerby M, Saxena SS, Smith RP, Skipper NT (2005) Superconductivity in the intercalated graphite compounds C6Yb and C6Ca. *Nat Phys* 1(1):39–41.
3. Mazin II (2005) Intercalant-driven superconductivity in YbC6 and CaC6. *Phys Rev Lett* 95(22):227001.
4. Calandra M, Mauri F (2005) Theoretical explanation of superconductivity in C6Ca. *Phys Rev Lett* 95(23):237002.
5. Yang S-L, et al. (2014) Superconducting graphene sheets in CaC6 enabled by phonon-mediated interband interactions. *Nat Commun* 5:3493.
6. Uchoa B, Castro Neto AH (2007) Superconducting states of pure and doped graphene. *Phys Rev Lett* 98(14):146801.
7. McChesney JL, et al. (2010) Extended van Hove singularity and superconducting instability in doped graphene. *Phys Rev Lett* 104(13):136803.
8. Profeta G, Calandra M, Mauri F (2012) Phonon-mediated superconductivity in graphene by lithium deposition. *Nat Phys* 8(2):131–134.
9. Nandkishore R, Levitov LS, Chubukov AV (2012) Chiral superconductivity from repulsive interactions in doped graphene. *Nat Phys* 8(2):158–163.
10. Guzman D, Alyahyaei H, Jishi R (2013) Superconductivity in graphene-lithium. arXiv: 1310.3813v1.
11. Fedorov AV, et al. (2014) Observation of a universal donor-dependent vibrational mode in graphene. *Nat Commun* 5:3257.
12. Margine ER, Giustino F (2014) Two-gap superconductivity in heavily n-doped graphene: Ab initio Migdal-Eliashberg theory. *Phys Rev B Condens Matter Mater Phys* 90(1):014518.
13. Bianchi M, et al. (2010) Electron-phonon coupling in potassium-doped graphene: Angle-resolved photoemission spectroscopy. *Phys Rev B Condens Matter Mater Phys* 81(4):041403.
14. Sugawara K, Sato T, Takahashi T (2008) Fermi-surface-dependent superconducting gap in C6Ca. *Nat Phys* 5(1):40–43.
15. Norman M, et al. (1998) Destruction of the Fermi surface in underdoped high-T_c superconductors. *Nature* 392(6672):157–160.
16. Mesot J, et al. (2001) Determination of the Fermi surface in high-T_c superconductors by angle-resolved photoemission spectroscopy. *Phys Rev B Condens Matter Mater Phys* 63(22):224516.
17. Evtushinsky DV, et al. (2009) Momentum dependence of the superconducting gap in Ba$_{1-x}$KxFe$_2$ As$_2$. *Phys Rev B Condens Matter Mater Phys* 79(5):054517.
18. Reber TJ, et al. (2012) The origin and non-quasiparticle nature of Fermi arcs in Bi$_2$ Sr$_2$ CaCu$_2$ O$_{8+\delta}$. *Nat Phys* 8(8):606–610.
19. Dynes R, Narayanamurti V, Garno J (1978) Direct measurement of quasiparticle-lifetime broadening in a strong-coupled superconductor. *Phys Rev Lett* 41(21): 1509–1512.
20. Veenstra CN, Goodvin G, Berciu M, Damascelli A (2010) Elusive electron-phonon coupling in quantitative analyses of the spectral function. *Phys Rev B Condens Matter Mater Phys* 82(1):012504.
21. Veenstra CN, Goodvin G, Berciu M, Damascelli A (2011) Spectral function tour of electron-phonon coupling outside the Migdal limit. *Phys Rev B Condens Matter Mater Phys* 84(8):085126.
22. Shi J, et al. (2004) Direct extraction of the Eliashberg function for electron-phonon coupling: A case study of Be(10$\bar{1}$0). *Phys Rev Lett* 92(18):186401.
23. Efros A, Shklovskii B (1975) Coulomb gap and low temperature conductivity of disordered systems. *J Phys Chem* 8:L49.
24. Davies JH, Franz JR (1986) Coulomb gap in sodium tungsten bronzes. *Phys Rev Lett* 57(4):475–478.
25. Massey JG, Lee M (1995) Direct observation of the coulomb correlation gap in a nonmetallic semiconductor, Si:B. *Phys Rev Lett* 75(23):4266–4269.
26. Raghu S, Kivelson SA, Scalapino DJ (2010) Superconductivity in the repulsive Hubbard model: An asymptotically exact weak-coupling solution. *Phys Rev B Condens Matter Mater Phys* 81(22):224505.
27. Nandkishore R, Thomale R, Chubukov AV (2014) Superconductivity from weak repulsion in hexagonal lattice systems. *Phys Rev B Condens Matter Mater Phys* 89(14): 144501.
28. Carbotte JP (1990) Properties of boson-exchange superconductors. *Rev Mod Phys* 62(4):1027–1157.
29. Valla T, et al. (2009) Anisotropic electron-phonon coupling and dynamical nesting on the graphene sheets in superconducting CaC6 using angle-resolved photoemission spectroscopy. *Phys Rev Lett* 102(10):107007.
30. Sanna A, et al. (2007) Anisotropic gap of superconducting CaC6: A first-principles density functional calculation. *Phys Rev B Condens Matter Mater* 75(2):020511.
31. Sanna A, et al. (2012) Phononic self-energy effects and superconductivity in CaC6. *Phys Rev B Condens Matter Mater Phys* 85(18):184514.
32. Gonnelli RS, et al. (2008) Evidence for gap anisotropy in CaC6 from directional point-contact spectroscopy. *Phys Rev Lett* 100(20):207004.
33. Kiss T, et al. (2007) Charge-order-maximized momentum-dependent superconductivity. *Nat Phys* 3(10):720.
34. Borisenko SV, et al. (2009) Two energy gaps and Fermi-surface "arcs" in NbSe2. *Phys Rev Lett* 102(16):166402.
35. Forti S, Starke U (2014) Epitaxial graphene on SiC: From carrier density engineering to quasi-free standing graphene by atomic intercalation. *J Phys D Appl Phys* 47(9): 094013.
36. Damascelli A (2004) Probing the electronic structure of complex systems by ARPES. *Phys Scr T* 109:61–74.
37. Grimvall G (1981) *The Electron-Phonon Interaction in Metals*, ed Wohlfart E (North-Holland, New York).

PHYSICS

Evidence for superconductivity in Li-decorated monolayer graphene

B.M. Ludbrook,[1, 2] G. Levy,[1, 2] P. Nigge,[1, 2] M. Zonno,[1, 2] M. Schneider,[1, 2]
D.J. Dvorak,[1, 2] C.N. Veenstra,[1, 2] S. Zhdanovich,[2, 3] D. Wong,[1, 2] P. Dosanjh,[1, 2]
C. Straßer,[4] A. Stöhr,[4] S. Forti,[4] C.R. Ast,[4] U. Starke,[4] and A. Damascelli[1, 2]

[1]*Department of Physics & Astronomy, University of British Columbia, Vancouver, British Columbia V6T 1Z1, Canada*
[2]*Quantum Matter Institute, University of British Columbia, Vancouver, British Columbia V6T 1Z4, Canada*
[3]*Department of Chemistry, University of British Columbia, Vancouver, British Columbia V6T 1Z1, Canada*
[4]*Max Planck Institute for Solid State Research, 70569 Stuttgart, Germany*

LITHIUM DEPOSITION ON MONOLAYER GRAPHENE

Lithium was deposited on monolayer graphene at a sample temperature of 8 K. Charge transfer from the Li electron dopes the graphene. At the saturation of doping, we find a sheet charge-carrier density $n_{2D} \simeq 9 \times 10^{13}\,\mathrm{cm}^{-2}$. Assuming Li forms an ordered LiC_6 structure after 4 minutes evaporation (i.e. one Li per three unit cells), this corresponds to a charge transfer to the graphene π^* bands of 0.14 ± 0.02 electrons per Li adatom. This is significantly lower than what is reported in Li-intercalated compounds, where the Li was found to be completely ionized [1], and results in the incomplete ionization of the Li-2s electrons. This is necessary in order to form a Li band at the Γ point, which in turn has been identified as an important element in the enhancement of the electron-phonon coupling [2–4].

The spectral weight at Γ that appears with the saturation of doping at low temperature is consistent with the superposition of a Li 2s band with a band folding due to a $\sqrt{3} \times \sqrt{3}\,R\,30°$ Li superstructure. On the one hand, the dispersion [see Fig. 1(d) in the paper] is reminiscent of a folded Dirac cone. On the other hand, the Fermi surface from 10-minute Li-decorated graphene in Fig.1(e) of the paper hints that the Li 2s band is also present at Γ, in addition to the folded π and π^* bands: the Fermi surface pocket at Γ is circular – and not 6-fold symmetric as expected for the folded Dirac bands – and its volume slightly larger, in agreement with calculations [2]. Disambiguation is difficult, as these bands all lie in the same energy and momentum region. Here we note simply that, empirically speaking, the spectral weight is present and it is important for the observation of the enhanced electron-phonon coupling (discussed below), and hence presumably also for the observation of the spectroscopic gap at the Fermi level.

EFFECTS OF TEMPERATURE

Increasing the temperature above 20 K leads to a progressive reduction of the charge transfer doping [Fig. S1(a) & Fig. S2], and at $\sim$50 K, to the disappearance of the backfolded spectral weight [Fig. S1(b)], arguably due to the complete disordering of the Li superstructure. The Γ point folded weight, and thus the Li ordering, do not reappear upon subsequent cooling. A significant broadening of the π^* bands with increasing temperature is also apparent, which again signifies increasing surface disorder due to the progressive degradation of the Li superstructure, as opposed to a damaging of the graphene sample itself; in fact, annealing to $\sim 300°$ C fully recovers the dispersion and linewidth of pristine graphene. For temperatures between 3.5 K and 20 K, the Li adatoms appear stable on the graphene surface. Fermi surfaces measured at 7 K, 13 K, and 17 K exhibit no change in volume within the bounds of uncertainty, as summarized in the evolution of the charge density n with temperature in Fig. S2.

We also see no evidence of the lithium intercalating beneath the graphene layer, in agreement with a previous study that found lithium to reside on top of monolayer graphene at temperatures around 50 K [5]. The strong temperature dependence of the doping seen here implies the Li atoms can become mobile above 20 K, typical of adatoms at a surface. This is in stark contrast with behaviour seen in Li-intercalated bulk graphite and bilayer graphene [1, 6], in which the doping from the intercalated lithium remains stable up to room temperature.

The enhancement of the electron-phonon coupling with increasing Li coverage can be reversed by increasing the temperature above 50 K, the point at which the spectral weight at Γ vanishes. Measurements were made on a 10 minute Li-decorated sample [Fig. S3(a)], and the same sample after annealing to 60 K for several minutes [Fig. S3(b)]. Both measurements were done at 8 K. After annealing, we see the near total disappearance of the low-energy renormalizations of the band, and the corresponding peak in Σ'. The contribution to $\alpha^2F(\omega)$ from below 100 meV is severely diminished, while the high energy part remains dominated by a double feature between 140 and 180 meV. The coupling is determined to be 0.13 ± 0.05, reduced from $\simeq 0.58$, and close to the value of the low-coverage sample.
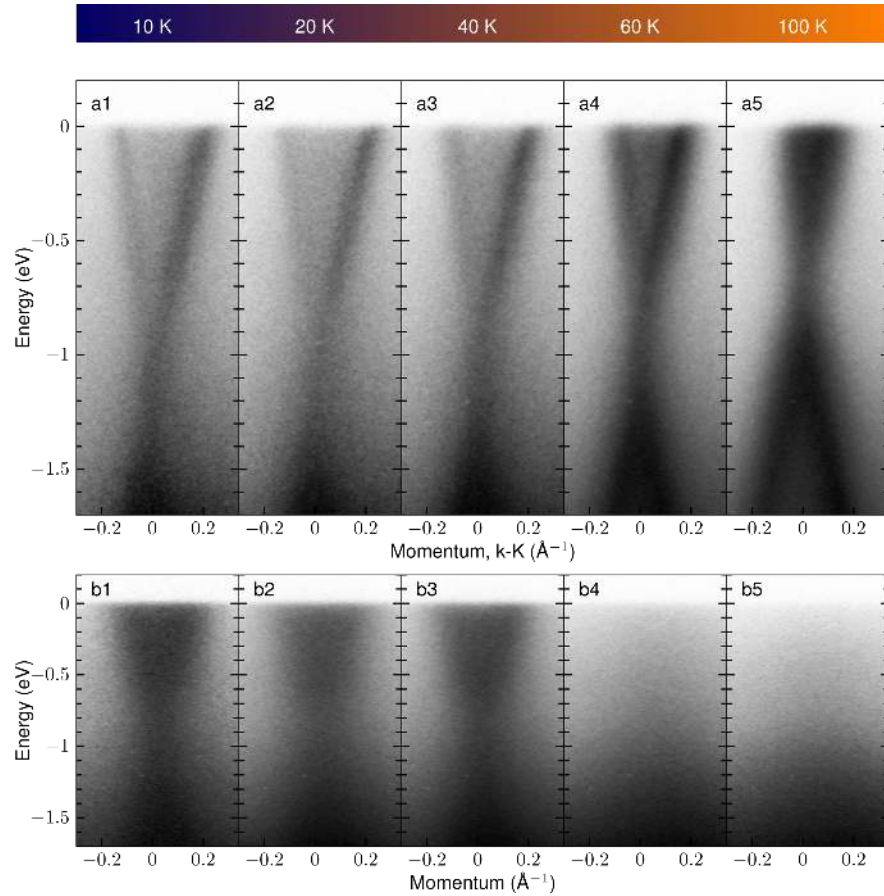
FIG. 1. **Temperature dependence of the band dispersion in Li-Graphene.** (a1-a5) ARPES measurements through the Dirac point at K showing a reduction in the n-type doping as the temperature is increased. A significant broadening of the bands can also be seen, particularly above 50 K, which is an indication of surface disorder. (b1-b5) ARPES measurements at Γ showing the complete disappearance of the spectral weight at 50 K.
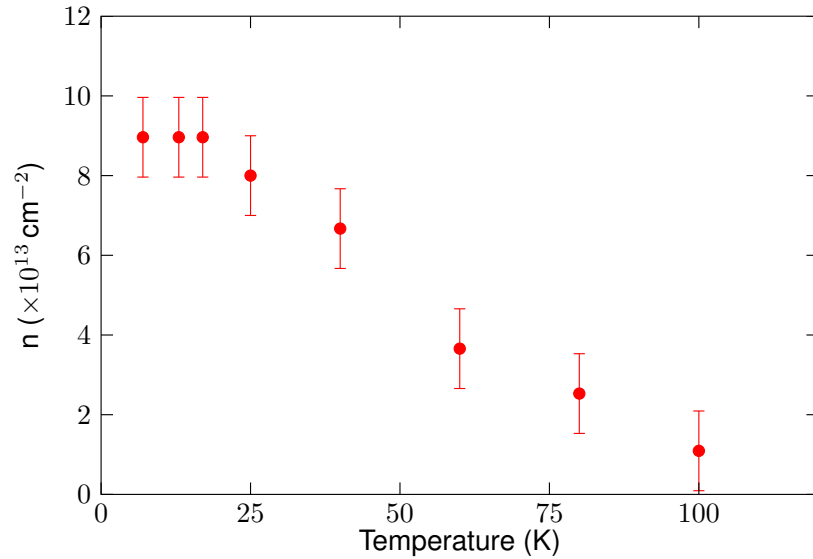

FIG. 2. **Evolution of the charge density n with temperature.** The charge density, determined from the Fermi surface volume of the graphene π^* bands, is shown for a graphene sample with 5-min. Li. At temperatures below $\sim$20 K the doping is stable. Above $\sim$20 K, however, there is a reduction of n with increasing temperature, with the sheet carrier density returning to the starting value of clean graphene ($1 \times 10^{13}\,\mathrm{cm^{-2}}$) at around 100 K.
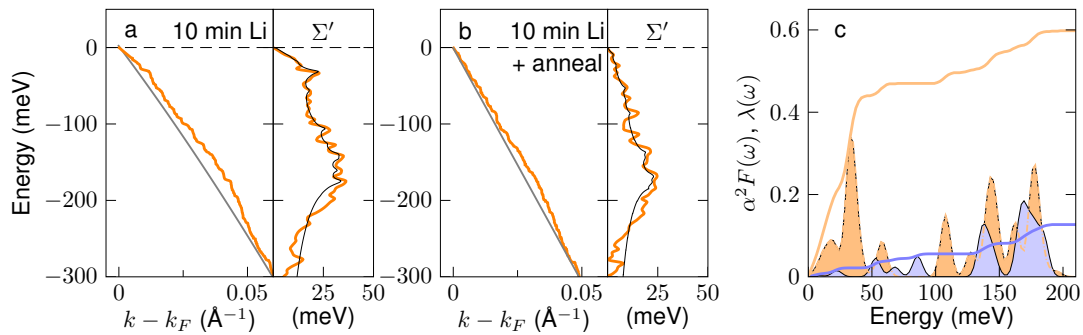
FIG. 3. **Reversible enhancement of the electron-phonon coupling.** The MDC dispersion (orange) and real part of the self energy (orange, right-hand panel) for the 10-minute Li sample in (a) show the strong kink at around 30 meV. (b) After annealing to 60 K for several minutes, the low energy feature is no longer apparent. (c) The Eliashberg functions corresponding to the fits to the self energy (black) in (a) and (b) are shown in light orange and light blue respectively. The absence of the low energy feature results in a severely diminished λ, shown as the solid lines in (c).

ANISOTROPY OF THE GAP

High-resolution measurements performed at the high symmetry point along K-M do not show a gap [Fig. S4]. The EDC of the Li-G at this point on the Fermi surface has its crossing point at 0, and the shape of the edge is the same as a reference measurement on polycrystalline gold. The slight difference in the slope of the edge crossing zero is attributed to a small difference in the experimental resolution between the two measurements. The gap is either closed or too small to measure with the resolution of this study. Either way, it demonstrates an anisotropy of the gap. This is perhaps not so surprising as bulk CaC_6 is thought to have an anisotropic superconducting gap [7–9].
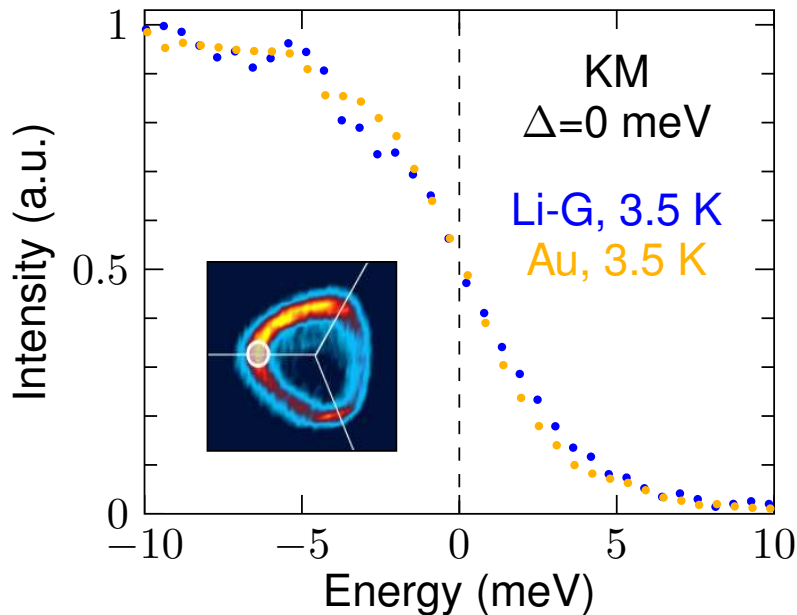

FIG. 4. **Absence of a gap along KM.** EDC at E_F at the corner of the triangular Fermi surface, as indicated by the white circle in the inset, for Li-Graphene (blue), as well as polycrystalline gold (yellow). Both measurements were done at 3.5 K.

SELF-ENERGY ANALYSIS

The spectral function measured by ARPES can be analyzed in terms of constant energy ($\omega = \tilde{\omega}$) momentum distribution curves (MDCs). The lineshape is Lorentzian, and can be fitted with [10]:

$$A_{\tilde{\omega}}(k) \simeq \frac{A_0}{\pi} \frac{\Delta k_m}{(k - k_m)^2 + (\Delta k_m)^2},$$ (1)

with

$$\Delta k_m = HWHM,$$ (2)

$$A_0 = \int A_{\tilde{\omega}}(k)dk.$$ (3)

The MDC dispersion is given by the peak maximum k_m at each energy, and is shown in Figs. S5(a-c) in black. The real and imaginary parts of the self-energy are related to these quantities by:

$$\Sigma'_{\tilde{\omega}} = \tilde{\omega} - \varepsilon^b_{k_m},$$
$$\Sigma''_{\tilde{\omega}} = -\Delta k_m v^b_{k_m},$$ (4)

where $\varepsilon^b_{k_m}$ is the energy of the bare-band at k_m and $v^b_{k_m}$ is the bare-band velocity. The self-energy thus depends on the choice of bare band, which is not known *a priori*. The bare-band is constrained to be a second order polynomial, and must coincide with the MDC dispersion at the Fermi level. Using the fact that the real and imaginary parts of the self-energy are Kramers-Kronig related, the bare-band parameters are varied until the quantities $\Sigma' - KK[\Sigma'']$ and $\Sigma'' - KK[\Sigma']$ are minimised, resulting in a self-consistent simultaneous determination of the bare-band and self-energy. The 'best fit' bare-band is shown in gray in Figs. S5(a-c), while the corresponding self-energies, and their KK transforms, are shown in orange and blue respectively, in panels (d)-(f).
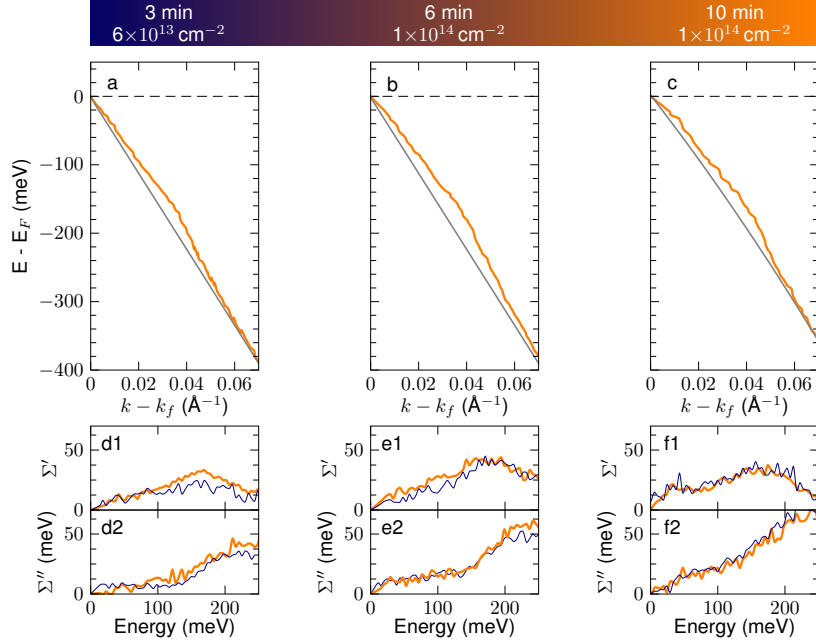

FIG. 5. **Self-consistent self-energy analysis.** MDC dipersions determined by fitting the ARPES data with Eqn. 1 plotted in orange in (a-c) are used to extract the self-energy using a self-consistent Kramers-Kronig procedure described. The bare-band [gray in (a-c)] corresponds to the real and imaginary parts of the self-energy calculated from Eqn. 4 plotted in orange in panels (d-f). The correct bare-band is identified by the good agreement between the real and imaginary parts of the self-energy, and their KK transforms (blue).

EXTRACTION OF ELIASHBERG FUNCTION

The real part of the self-energy is related to the bosonic spectrum by

$$\Sigma'(\mathbf{k}, \omega) = \int_0^\infty d\omega' \, \alpha^2 F(\mathbf{k}, \omega') \, K\left(\frac{\omega}{kT}, \frac{\omega'}{kT}\right) , \tag{5}$$

where $K(y, y') = \int_{-\infty}^{+\infty} dx \, f(x-y) \, 2y'/(x^2 - y'^2)$ and $f(x-y)$ is the Fermi-Dirac distribution. The momentum resolved $\alpha^2 F(\omega)$ function is extracted from the self-energy by an integral inversion procedure using a maximum entropy method (MEM) [11]. The results of this fitting procedure can be seen in Fig. S6 where the $\alpha^2 F(\omega)$ in panels (g-i) correspond to the very good fits to Σ' in the lower panels of (d-f), and the corresponding calculated MDC dispersion (black) in panels (a-c). The KK transform of the fit to Σ' is compared to the experimental Σ'' in panels (d2-f2) and the agreement is good, with the dominant steps occurring at energy of the peaks in $\alpha^2 F(\omega)$.

The momentum-resolved electron-phonon coupling strength is defined as [12]:

$$\lambda_{\mathbf{k}}(\omega) = 2 \int_0^\omega d\omega' \, \frac{\alpha^2 F(\mathbf{k}, \omega')}{\omega'} , \tag{6}$$

As a consistency check on the analysis and extraction of the electron-phonon coupling strength, we have done a parallel analysis of the 6-minute Li-decorated sample using a simplified model of $\alpha^2 F(\omega)$ consisting of four Lorentzians whose position, width, and area can be varied in order to simultaneously fit the real and imaginary parts of the self-energy. The $\alpha^2 F(\omega)$ found with this method is in good agreement with that found by the maximum-entropy method, with the main peaks at the same energies. The resulting $\lambda = 0.55 \pm 0.05$ is slightly larger than the value from the maximum-entropy method (0.46 ± 0.05), an effect that has been previously observed when comparing these analysis
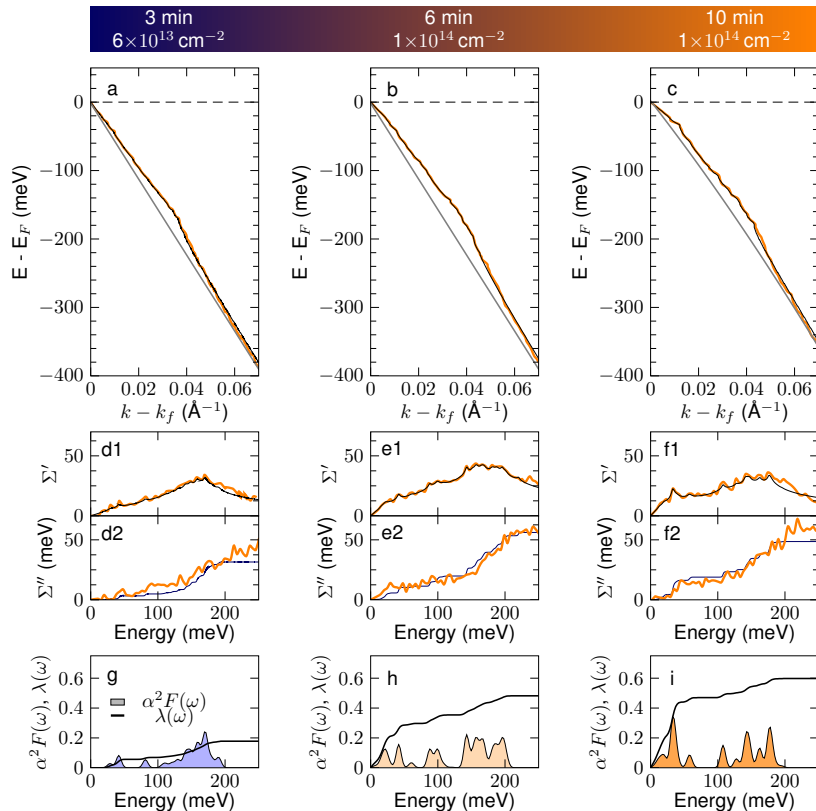
FIG. 6. **Self-energy and determination of the Eliashberg function.** The MDC dispersion (black) and bare band (gray) from the KKBF routine are shown in panels (a-c), while the real and imaginary parts of the self-energy are shown in orange in panels (d-f). The maximum entropy method inversion results in an excellent fit to Σ' (black, d1-f1) and it's KK transform (blue) compares favourably with Σ'' (orange). The Eliashberg functions from each fit are plotted in panels (g-i). Using the results of the fits, the dispersion can be calculated, and is shown in black in panels (a-c).

methods in other materials [13]. The Lorentzian method is less sensitive to the details of the MDC dispersion, and hence less sensitive to the noise in the data. In this sense, it is a good consistency check on the maximum-entropy method analysis. However, given its tendency to overstate the value of λ, we focus primarily on the more conservative results from the maximum-entropy method.
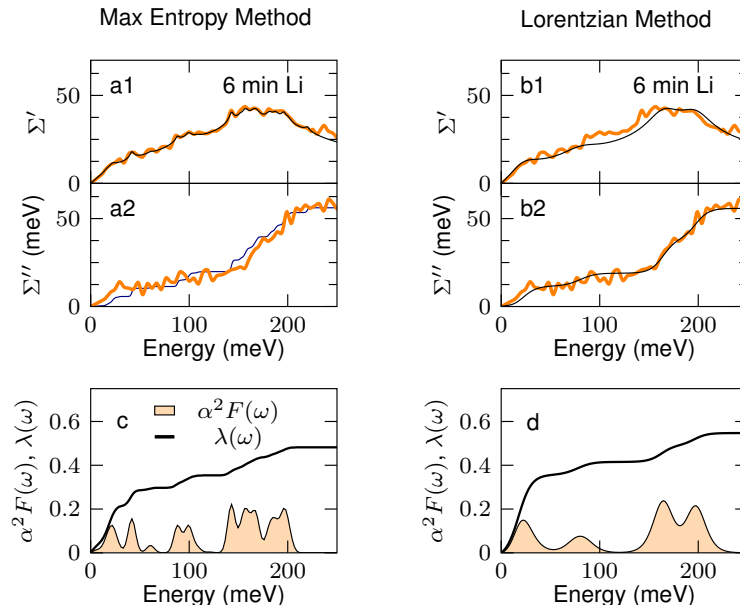

FIG. 7. **Comparison of two methods for determining $\alpha^2F(\omega)$ and λ.** The real and imaginary parts of the self-energy for the 6-minute Li-decorated sample are shown in orange in (a) and (b). The maximum-entropy method is used to fit Σ' in black in (a1), and its Kramers-Kronig transform is shown in blue in (a2). The Eliashberg function and electron-phonon coupling constant λ are shown in (c). An alternate method for extracting $\alpha^2F(\omega)$ by simultaneously fitting the real and imaginary parts of the self-energy with equal weighting is shown in (b). The Eliashberg function, which consists of four Lorentzians whose position and size is varied to achieve a good fit, is shown in (d), along with λ.

[1] Sugawara, K., Kanetani, K., Sato, T. & Takahashi, T. Fabrication of Li-intercalated bilayer graphene. *AIP Adv.* **1**, 022103 (2011).
[2] Profeta, G., Calandra, M. & Mauri, F. Phonon-mediated superconductivity in graphene by lithium deposition. *Nat. Phys.* **8**, 131–134 (2012).
[3] Calandra, M. & Mauri, F. Theoretical explanation of superconductivity in C$_6$Ca. *Phys. Rev. Lett.* **95**, 237002 (2005).
[4] Csányi, G., Littlewood, P. B., Nevidomskyy, A. H., Pickard, C. J. & Simons, B. D. The role of the interlayer state in the electronic structure of superconducting graphite intercalated compounds. *Nat. Phys.* **1**, 42–45 (2005).
[5] Fedorov, A. V. *et al.* Observation of a universal donor-dependent vibrational mode in graphene. *Nat. Comm.* **5**, 3257 (2014).
[6] Watcharinyanon, S., Johansson, L., Zakharov, A. & Virojanadara, C. Studies of Li intercalation of hydrogenated graphene on SiC(0001). *Surf. Sci.* **606**, 401–406 (2012).
[7] Sanna, A. *et al.* Anisotropic gap of superconducting CaC$_6$: A first-principles density functional calculation. *Phys. Rev. B* **75**, 020511 (2007).
[8] Sanna, A., Pittalis, S., Dewhurst, J. & Monni, M. Phononic self-energy effects and superconductivity in CaC$_6$. *Phys. Rev. B* **85**, 184514 (2012).
[9] Gonnelli, R. *et al.* Evidence for Gap Anisotropy in CaC$_6$ from Directional Point-Contact Spectroscopy. *Phys. Rev. Lett.* **100**, 207004 (2008).
[10] Veenstra, C. N., Goodvin, G., Berciu, M. & Damascelli, A. Spectral function tour of electron-phonon coupling outside the Migdal limit. *Phys. Rev. B* **84**, 21–25 (2011).
[11] Shi, J. *et al.* Direct Extraction of the Eliashberg Function for Electron-Phonon Coupling: A Case Study of Be(1010). *Phys.l Rev. Lett.* **92**, 186401 (2004).
[12] Grimvall, G. *The Electron-Phonon Interaction in Metals* (edited by E. Wohlfart, North-Holland, New York, 1981).
[13] Chien, T., Rienks, E. D. L., Jensen, M. F., Hofmann, P. & Plummer, E. W. Anisotropic electron-phonon coupling on a two-dimensional circular Fermi contour. *Phys. Rev. B* **80**, 241416 (2009).